CrossMark

A valence states approach for luminescence enhancement by low dopant concentration in Eu-doped ZnO nanoparticles

A. Mesaros[1] · D. Toloman[2] · M. Nasui[1] · R. B. Mos[1] · T. Petrisor[1] ·
B. S. Vasile[3] · V. A. Surdu[3] · I. Perhaita[4] · A. Biris[2] · O. Pana[2]

Abstract The paper presents a simple, reproducible, controllable, and direct wet chemical synthesis method for $Zn_{1-x}Eu_xO$ nanoparticles. The full understanding of decomposition mechanism of the as-obtained oxalate precipitate was achieved based on the thermal analysis correlated with the evolved gas analysis and FTIR spectroscopy. The structure, morphology, and optical luminescent properties of the $Zn_{1-x}Eu_xO$ nanoparticles have been investigated by X-ray diffraction, Raman spectroscopy, HRTEM, SAED, XPS, and PL. The XRD studies reveal the formation of a hexagonal wurtzite-type structure. The presence of Eu_2O_3 cubic structure can be observed up to 0.5 mol% Eu, suggesting that the solubility of the divalent or trivalent Eu into the ZnO lattice is limited. The formation of Eu_2O_3 secondary phase at higher Eu concentration is sustained by Raman spectroscopy and XPS, as well. The TEM investigations of the Eu-doped ZnO samples illustrate the presence of aggregates with different shapes and dimensions formed by agglomerated spherical and polyhedral nanoparticles with sizes ranging from 20 to 120 nm. The effect of europium concentration on the structural and morphological characteristics, as well as on the luminescent properties was studied with special emphasis on the europium chemical states—Eu^{2+} and Eu^{3+}. The PL measurements sustain the presence of both divalent and trivalent europium ions into the ZnO host lattice and, at the same time, an increase of its defects density induced by the dopant presence.

Introduction

The ZnO nanoparticles are of great interest for researchers due to their potential applications in ultraviolet (UV) to blue-violet light-emitting devices [1–3], photocatalysis [4, 5], dye-sensitized solar cell [6], diluted magnetic semiconductors [7, 8], etc. It is already well known that the optical properties of ZnO nanoparticles can be modulated by doping the ZnO matrix with different metal ions, i.e., classical $3d$ transition metals or rare earth metals, and/or by modifying the morphological characteristics [9, 10]. Compared to transition metals, rare earth ions generate efficient luminescent centers due to their $4f$ intrashell transitions that exhibit peculiar narrow and intense emission lines [11, 12]. Among the rare earth elements, europium is special as a dopant because it can induce different luminescent characteristics depending on the oxidation states +2, or +3. The luminescent emission of Eu^{3+} is specific due to the $4f \rightarrow 5d$ transitions, and is centered at around 612 nm in the red domain. On the other hand, the luminescent emission of Eu^{2+} is due to the dipole allowed $5d$–$4f$ transition and varies in a wide range from red to ultraviolet depending on the crystal structure of the host matrix [12]. It has been reported that only at smaller concentration (less than 1 molar %) the divalent europium

✉ D. Toloman
dana.toloman@itim-cj.ro

1 Physics and Chemistry Department, Technical University of Cluj-Napoca, 28 Memorandumului Street, 400114 Cluj-Napoca, Romania

2 National Institute for Research and Development of Isotopic and Molecular Technologies, 65-103 Donath Street, 400293 Cluj-Napoca, Romania

3 Faculty of Applied Chemistry and Material Science, University "Politehnica" from Bucharest, 1-7, Gh. Polizu Street, 011061 Bucharest, Romania

4 Raluca Ripan Institute for Research in Chemistry, Babes-Bolyai University, Fantanele 30, 400294 Cluj-Napoca, Romania

ions are successfully substituting Zn^{2+} in the ZnO host matrix [13]. At higher europium concentration, the structural investigations have pointed out the presence of Eu_2O_3 at the surface of ZnO [13]. Recently, Yang and co-workers have evidenced that at smaller Eu concentration (1–3 mol%) a great number of defects are generated in the ZnO lattice, such as oxygen vacancy (V_O), or interstitial oxygen (O_i), and these defects play an important role in the energy transfer process from the host lattice to Eu^{3+} [14]. Also, it has been reported that the optical properties of the metal-doped zinc oxide strongly depends on the particles size, shape, and the surrounding environment [15–17].

Different synthesis methods, such as solid-state reaction [18], coprecipitation [19–21], sol–gel [22–24], hydrothermal [25–27], pyrosol [28, 29], microemulsion [30–32], combustion [13], and electrochemical methods [33, 34] have been used in order to obtain the europium-doped zinc oxide nanoparticles. The precipitation/coprecipitation method, as compared to other chemical or physical methods, is an inexpensive method which allows the synthesis of a wide range of nanoparticles with different and controlled sizes and shapes [19, 20, 35–37].

The paper presents a simple, reproducible, controllable, and direct wet chemical synthesis method for $Zn_{1-x}Eu_xO$ ($x = 0.001, 0.005, 0.01, 0.025$) nanoparticles, which consists in the addition of reactants as acetate salts and oxalic acid, under pH control, in the presence of an anti-agglomeration agent. The effect of europium concentration on the structural and morphological characteristics, as well as on the optical luminescent properties was studied with special emphasis on the europium chemical states—Eu^{2+} and Eu^{3+}. In this regard, complementary investigation techniques were used to evidence the presence of divalent europium into the ZnO matrix and to reveal its effect on the luminescent properties.

Experimental part

The nanocrystalline $Zn_{1-x}Eu_xO$ ($x = 0.001, 0.005, 0.01, 0.025$) samples were prepared by the wet chemical synthesis route—simultaneous addition of reagents (WCS-SimAdd), using zinc acetate dihydrate, $Zn(CH_3COO)_2 \cdot 2H_2O$ and europium nitrate hydrate, $Eu(NO_3)_3 \cdot xH_2O$ (99.9 %, Alfa Aesar) as the corresponding starting salts and oxalic acid dihydrate, $H_2C_2O_4 \cdot 2H_2O$ as precipitating reagent. 0.5 M aqueous solutions of salts and 0.5 M oxalic acid were prepared. The precipitation was carried out under continuous magnetic stirring and the pH value was adjusted to 8 ± 0.2, by adding an ammonium hydroxide solution, NH_4OH. Also, tetraethylammonium hydroxide,

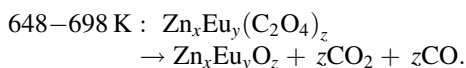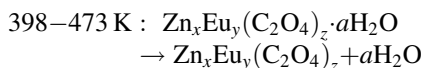$(C_2H_5)_4N(OH)$ was used as an anti-agglomeration agent. The post-precipitation stage consisted in a 24 h aging, separation by filtering and drying. The precursor thermal treatment was performed at 773 K, for 2 h, in air at a heating rate of 300 K/h.

The as-obtained precursors were characterized by thermogravimetric and differential thermal analysis (Mettler Toledo TGA/SDTA851; platinum crucible, heating rate 10 K/min; nitrogen flow 30 ml/min); evolved gas analysis (Thermo Scientific Nicolet 6700 FTIR Spectrometer equipped with a TGA module, working at 150 °C; HR Nicolet TGA Vapor phase library). Bright-field and high-resolution transmission electron microscopy images (TEM/HRTEM) coupled with selected area electron diffraction (SAED) were obtained using a 300 kV Tecnai G^2 F30 S-TWIN transmission electron microscope from FEI, the Netherlands. The X-ray diffraction (XRD) measurements were made using a Bruker D8 Advance diffractometer with Cu X-ray tube and incident beam Ge (111) monochromator ($\lambda = 1.54056$ Å). Raman analysis was performed at room temperature using a spectrophotometer Jasco (NRS 3300) arranged in a back-scattering geometry and equipped with a charge-coupled device detector (-69 °C) which uses a 600 l/mm grid allowing a spectral resolution of 14.66 cm^{-1}. The laser incident beam (approximate size 1 μm^2) was focused on the sample surface through an Olympus microscope with a 100× objective. The instrument was calibrated based on the Si 521 cm^{-1} peak. The laser excitation was conducted using a 514.5 nm argon ion laser, and the power at the surface of the sample was maintained at 1.6 mW, the exposure time (t_e) was different (10–60 s) to maximize the signal and is inserted in the Raman figures for each sample. The qualitative and quantitative sample compositions were investigated using X-Ray Photoelectron Spectroscopy (XPS) assisted by Ar ions etching. The XPS spectra were recorded using a SPECS spectrometer working with an Al anode (1486.6 eV) as X-rays source. The spectrometer is equipped with a PHOIBOS 150 analyzer, microchannel plate photomultiplier, and CCD detector, ensuring a 0.8 eV resolution on the Ag 3d line. The pass energy was set to 0.1 eV. Each sample was subjected to several Ar ions etchings until the XPS spectra remained unchanged in shape and intensity. At this stage, the XPS spectra reflect the real composition of the samples. In order to avoid the artificial reduction of the different oxidation stats of elements, the etching was performed by using Ar ions accelerated at a maximum 1000 V voltage [38]. The luminescent characterization was performed by using a JASCO FP-6500 Spectrofluorimeter Wavel; glass filter WG 320.

Results and discussion

Thermal analysis

Considering that the critical step in the synthesis by wet chemical methods is the thermal decomposition of the precursor, thermogravimetric and differential thermal analyses (TG–DTA) and TG coupled with FTIR analyses (TG–FTIR) were conducted to better understand the thermal behavior of the (Zn,Eu)-oxalate-type precursors. The DG–DTA curves registered for the ZnO:Eu samples are similar, Fig. 1 presents the thermal analysis of $Zn_{0.999}$ $Eu_{0.001}O$ sample. The TG–DTA analyses have revealed that the decomposition of the precursors takes place in two successive stages. All the samples present the first decomposition stage in the temperature range of 398–473 K with a mass loss of around 19 wt% attributed to the elimination of the physically adsorbed water. The main decomposition process, corresponding to the exothermic effect observed between 648 and 698 K with a significant mass loss at around 38 wt%, is attributed to the decomposition of the oxalate group. Thus, it can be assumed that the decomposition of the precipitates takes place according to the general reaction scheme for the oxalate route:

$$398-473\,K:\ Zn_xEu_y(C_2O_4)_z\cdot aH_2O \rightarrow Zn_xEu_y(C_2O_4)_z + aH_2O$$

$$648-698\,K:\ Zn_xEu_y(C_2O_4)_z \rightarrow Zn_xEu_yO_z + zCO_2 + zCO.$$

No significant weight loss was observed for temperatures higher than 773 K in the TG curves, indicating that the oxalate intermediates were completely decomposed.

TG-FTIR analysis

Figure 1 presents the 3D plot for FTIR absorbance time dependence of the evolved gases for the $Zn_{0.999}Eu_{0.001}O$ sample. The FTIR profile of the gas evolved at different times/temperature is also depicted. The two main decomposition stages are accompanied by a major gas release. The FTIR characteristic absorbance bands of the gaseous products—H_2O, CO_2, and CO can be observed: $v_{O-H} \sim 3400$–4000 cm^{-1}, $\delta_{O-H} \sim 1300$–1900 cm^{-1} for H_2O; $v_{CO} \sim 2360$ cm^{-1} for CO_2; $v_{CO} \sim 2184$, 2110 cm^{-1} for CO [39, 40]. In the temperature range 398–473 K (FTIR spectrum at minute 13–14), the released gases consist of H_2O—physically adsorbed water—and CO_2, adsorbed from the atmosphere. As the thermal treatment continues and the temperature increases, all the precursors simultaneously release CO_2 and CO (FTIR spectra at minute 37–38, 670–671 K) due to the decomposition of zinc oxalate.

X-ray diffraction

Figure 2 shows the XRD patterns of the undoped ZnO and the Eu-doped ZnO nanoparticles with different doping concentrations (0.1–2.5 mol%). It is found that all the samples possess a typical hexagonal wurtzite structure by comparison with the data from JCPDS standard file—PDF No. 36-1451, space group $P6_3mc$ (186). No diffraction peaks from any other chemical species, such as Eu_2O_3, are detectable in the diffraction pattern of the 0.1 mol% Eu-doped sample. By analyzing the XRD patterns, one can observe that by increasing the Eu concentration (up to 0.5 mol%) a weak diffraction line at 28.423°, belonging to Eu_2O_3 phase, can be detected. The Eu_2O_3 cubic structure
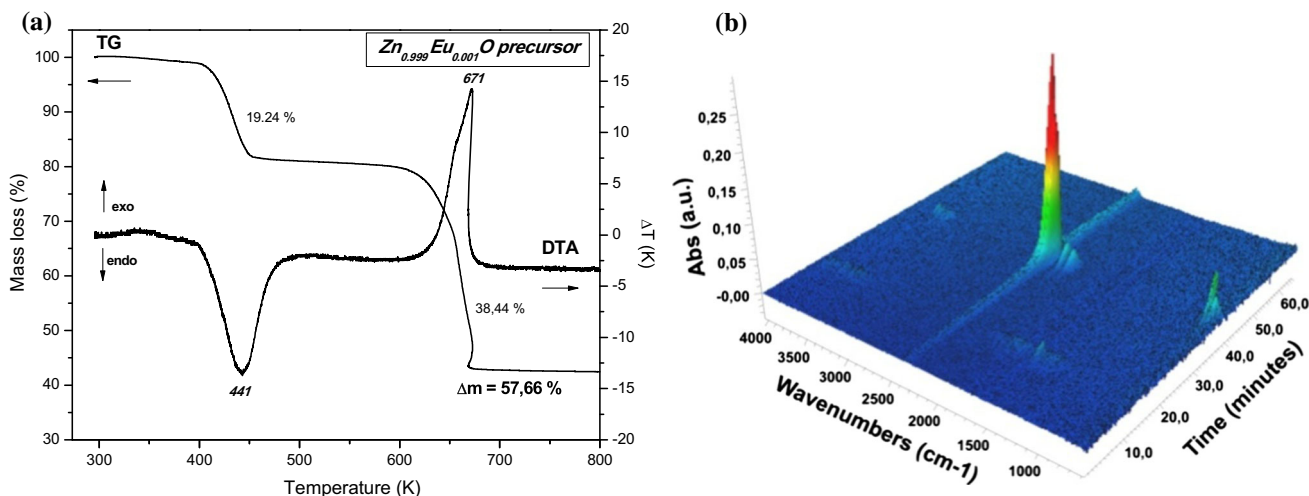
Fig. 1 TG–DTA curves of $Zn_{0.999}Eu_{0.001}O$ sample (a) and 3D image for the variation in time of the FTIR absorbance of gases released from the decomposition of the same sample (b)
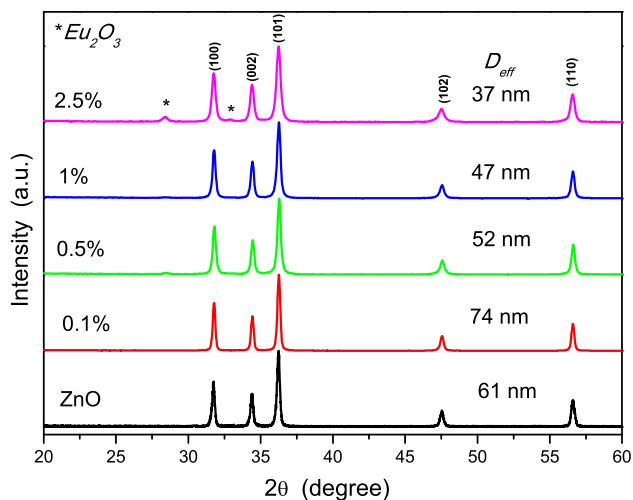
Fig. 2 XRD patterns of ZnO and Eu-doped ZnO nanoparticles (x mol% Eu)

appears as a second phase, indicating that the solubility of Eu^{3+} ions into the ZnO host matrix is below 0.5 mol%.

The calculated values for the ZnO crystallite sizes (D_{eff}), calculated using the Scherrer formula are presented in Fig. 2. The average crystallite sizes, calculated for the (101) and (100) peaks, were about 61 nm for undoped ZnO. For the 0.1 mol% Eu, the crystallite size has increased to 74 nm, indicating that this small amount of europium ions stimulates the nucleation, and the growth processes of the nanocrystals.

At higher europium concentration, a decrease of the crystallite size can be noticed—down to 37 nm for the 2.5 mol% Eu. This tendency can be correlated with the segregation of the Eu_2O_3 phase, probably at the nanoparticles surface, inhibiting thus the ZnO nanocrystal growth process. Even if the Eu_2O_3 specific diffraction lines are distinguished only at higher dopant concentration (more than 1 mol%), the decrease of crystallite size values can be associated with the lower solubility of Eu ions into the ZnO lattice [11]. Due to the lower intensity of the Eu2O3 reflection lines, the average nanoparticles sizes have been calculated using the Scherrer formula, only for the 1 and 2.5 % mol Eu samples and the obtained values are 14 and 24 nm, respectively.

Raman spectroscopy

To obtain detailed information about the composition of the samples, Raman spectroscopy measurements were performed. Figure 3a shows Raman spectra of ZnO, Eu-doped ZnO nanoparticles, and Eu_2O_3 in the range 150–800 cm^{-1}. The space group of hexagonal ZnO, with a wurtzite crystal structure belongs to the C_{6v}^4. Single crystalline ZnO presents eight sets of optical phonon modes in

which the $A_1 + E_1 + 2E_2$ modes are Raman active, while the A_1 and E_1 modes split into longitudinal optical (LO), and transverse optical (TO) components. The Raman spectrum of the ZnO nanoparticles presents peaks at 338, 395, 447, 587, and 666 cm^{-1}. The bands at 338 and 395 cm^{-1} are assigned as the $2E_{2L}$ and the TO mode with A_1 symmetry (A_{1T}), respectively. The peak centered at 447 cm^{-1} is attributed to the E_{2H} mode of the ZnO nonpolar optical phonons [41, 42]. The bands at 587 cm^{-1} correspond to the E_1 symmetry with LO modes. Generally, the $E_1(LO)$ peak is caused by defects due to O-vacancies, Zn-interstitials [43, 44]. The peak centered at 666 cm^{-1} was assigned to two phonon processes $A_1(LO) + E_2(low)$ [45].

By doping ZnO with Eu ions it can be observed that the bands characteristic to ZnO are decreasing with the doping degree. Moreover, the Raman peaks of E_{2H} evidently shift toward a lower wavenumber from 447 cm^{-1} for the undoped ZnO to 444 cm^{-1} for the 0.1 mol% Eu-doped ZnO, confirming an effective substitution of Zn^{2+} ions by Eu^{2+} ions. It can be observed that this band returns to its initial position by increasing the dopant concentration. Also, by increasing the doping level, the band centered at 338 cm^{-1} is shifting to higher wavenumbers, 342 cm^{-1} for 2.5 mol% Eu-doped ZnO nanoparticles. The Raman spectrum of the Eu_2O_3 sample presents a characteristic band at 346 cm^{-1}, specific to a Tg mode. Thus, the bands centered at $\sim$342 cm^{-1} could be assigned to both ZnO, and Eu_2O_3.

Figure 3b presents the Raman spectra of ZnO, Eu-doped ZnO nanoparticles, and Eu_2O_3 in the wavenumber range 2000–8000 cm^{-1}. In this range, only the Eu-doped ZnO nanoparticles present bands and these bands are specific to Eu_2O_3 [46]. It should be noted here that for 0.1 mol% Eu all these bands exhibit low intensities, while for higher concentrations these bands are better resolved. Taking into consideration all these results, one can conclude that at smaller concentration, 0.1 mol%, a part of Eu^{3+} ions are reduced to Eu^{2+} and are incorporated into ZnO lattice and the others contribute to the formation of Eu_2O_3 species. The formation of Eu_2O_3 secondary phase at higher Eu concentration is sustained by XRD analysis, as well.

TEM–HRTEM analysis

The TEM analysis (Fig. 4a) obtained on the precursor powder provides a direct observation of the morphological and structural characteristics. The precursor powder consists in agglomerated nanocrystalline particles, this behavior being characteristic for the oxalate-type precursors [21, 37, 47, 48]. The high-resolution pattern (Fig. 4b) clearly illustrates the amorphous character, but also the presence of very small nanocrystalline particles (4–5 nm in size).
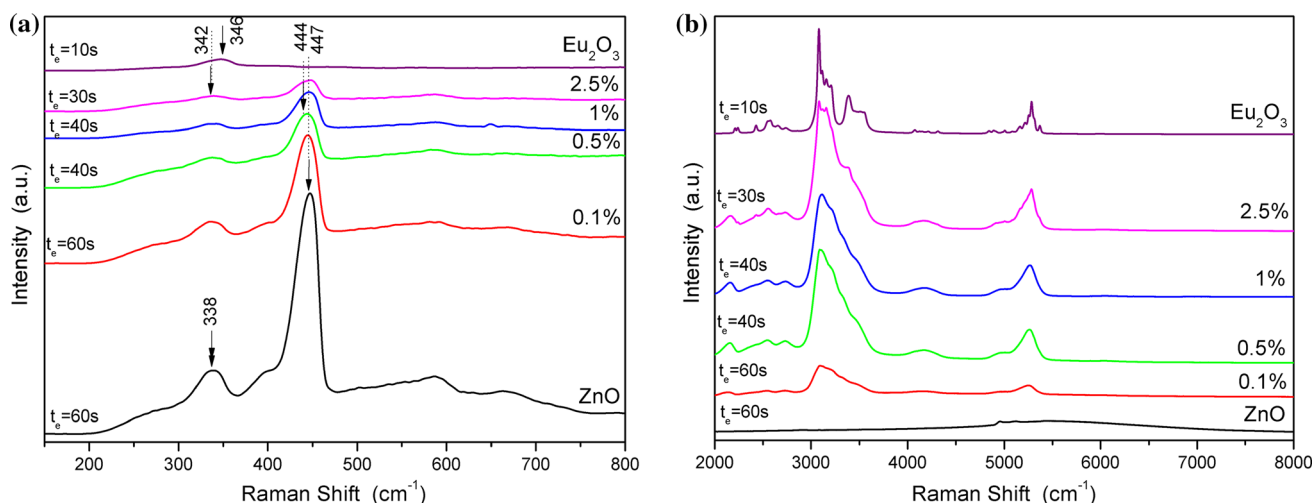
Fig. 3 Raman spectra of ZnO, Eu-doped ZnO nanoparticles, and Eu_2O_3 in the 150–800 cm^{-1} (**a**) and 2000-8000 cm^{-1} (**b**) ranges

Fig. 4 TEM image (**a**) and HRTEM pattern (**b**) of $Zn_{0.975}Eu_{0.025}O$ precursor
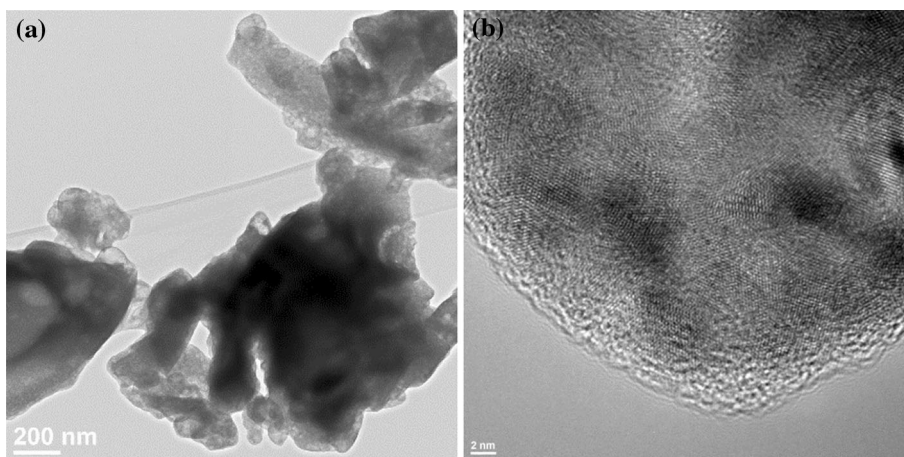
The **TEM** bright-field images of Eu-doped ZnO samples (Fig. 5a–c) illustrate the presence of aggregates with different shapes and dimensions formed by agglomerated spherical and polyhedral nanoparticles with sizes ranging from 20 to 120 nm.

This tendency to form larger and denser nanoparticle aggregates during the thermal treatment is typical for zinc oxalate-type precursors [48]. Moreover, the particle size distribution (Fig. 5g–i) histograms for these samples point out the influence of Eu dopant on the mean particle size in terms of decreasing the particle size with the increase of Eu content. The SAED patterns (Fig. 5a–c inset) are in good agreement with the X-ray diffraction patterns and show a wurtzite crystal structure (JCPDS standard file—PDF No. 36-1451) for all the doped samples.

HRTEM images (Fig. 5d–f) show clear lattice fringes of polycrystalline nanopowder with $d = 2.81$ Å, $d = 2.60$ Å, $d = 2.47$ Å, $d = 1.91$ Å, and $d = 1.62$ Å corresponding to

the (100), (002), (101), (102), and (110) crystallographic planes of hexagonal ZnO.

XPS

The quantitative analysis of samples, as well as the determination of Eu ions valence states was performed by XPS coupled with Ar ions etching. The following XPS core-level lines were consecutively recorded after different etching time intervals: Eu 3d, Zn 2p, and C 1s. The C 1s line associated to C–C or C–H bonds positioned at 284.6 eV was used for spectra calibration. The C 1s line is due to the carbon presence in the outer shell of nanoparticles, as resulted from the thermal decomposition of non-reacted precursor traces.

The presence of both oxidation states of Eu can be explained by taking into consideration the reducing character of the oxalate-type species. The analysis of XPS
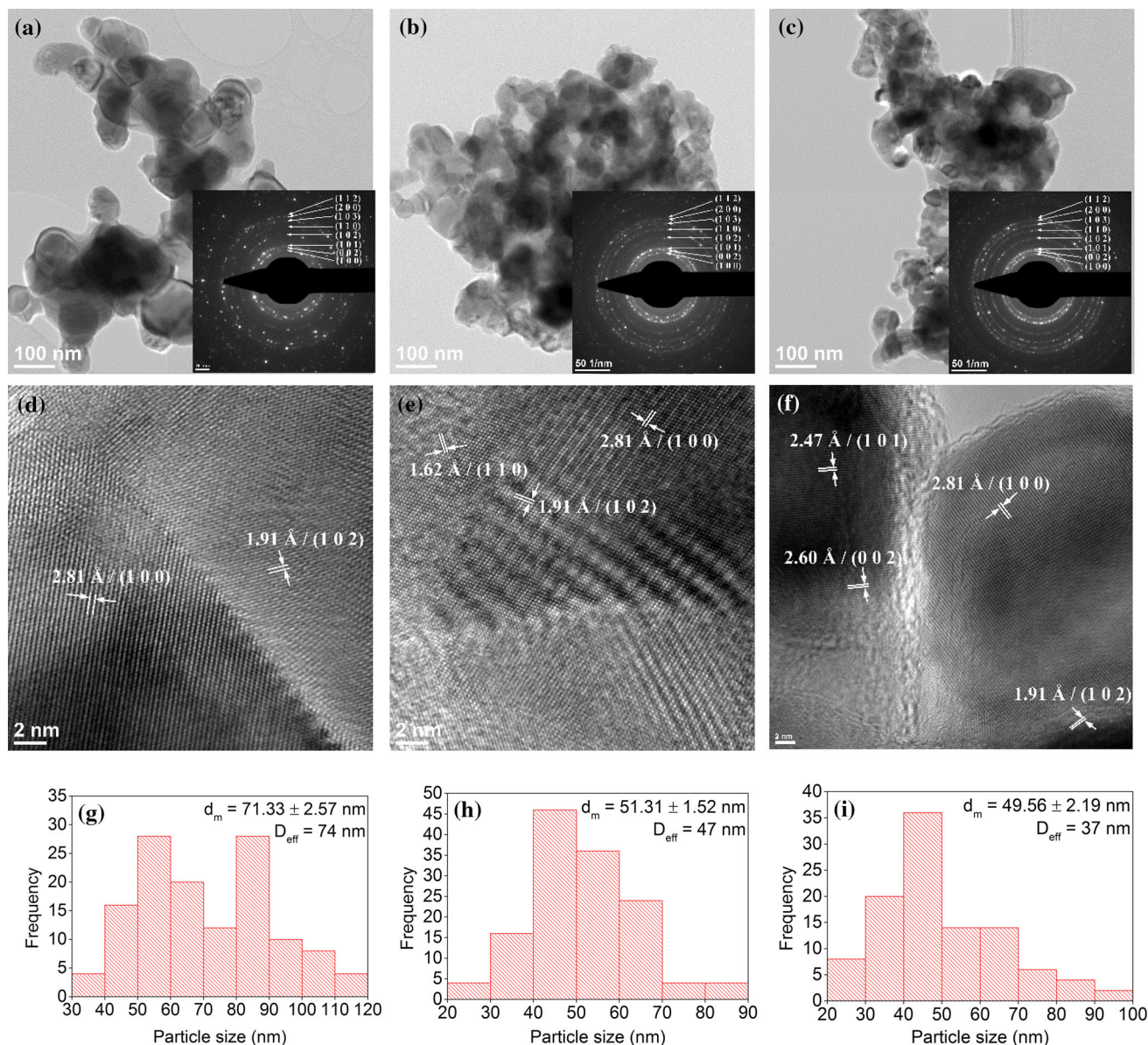
Fig. 5 Bright-field TEM images and SAED pattern (*inset*) (**a–c**), HRTEM images (**d–f**), particle size distribution (**g–i**) of $Zn_{0.999}Eu_{0.001}O$, $Zn_{0.99}Eu_{0.01}O$, and $Zn_{0.975}Eu_{0.025}O$, respectively

spectra of Eu $3d$ was made considering that both Eu^{2+} and Eu^{3+} are present. According to the Raman spectra, the divalent component of europium is expected, and corresponds to the europium ions that substitute the Zn^{2+} ions into the ZnO host lattice. On the other side, the presence of Eu^{3+} ions may be either due to the interstitial incorporation of Eu ions into the ZnO matrix, or to the formation of Eu_2O_3 as a secondary phase. It is important to notice that the XRD evidences the formation of Eu_2O_3 phase at a dopant concentration higher than 1 mol%.

The fit was realized by using the CASA software. A Shirley background was set for all spectra, except for the Eu $3d$ core-level lines where a linear one is more suitable.

The satellites were extracted through the CASA software designed setup. The restrictions used for fitting the Eu $3d$ and Zn $2p$ XPS spectra refer to the relation between the integral intensities of the doublet components $I_{(3/2)} = (2/3) I_{(5/2)}$ and $I_{(1/2)} = (1/2) I_{(3/2)}$ for d and p lines, respectively. The $3d$ and $2p$ spin–orbit doublet separations were considered at 29.6 and 23 eV for Eu $3d$ and Zn $2p$, respectively. After repeated Ar ions etchings, the XPS spectra remained unchanged in shape and intensity, being suitable for quantitative determinations.
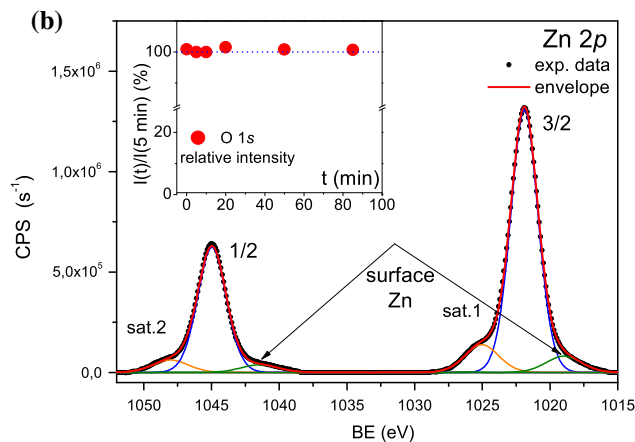
The XPS spectra of Eu $3d$ core-level doublet for 2.5 mol% Eu-doped ZnO nanoparticles together with the corresponding deconvolutions and fitted curves are shown

(a)

(b)
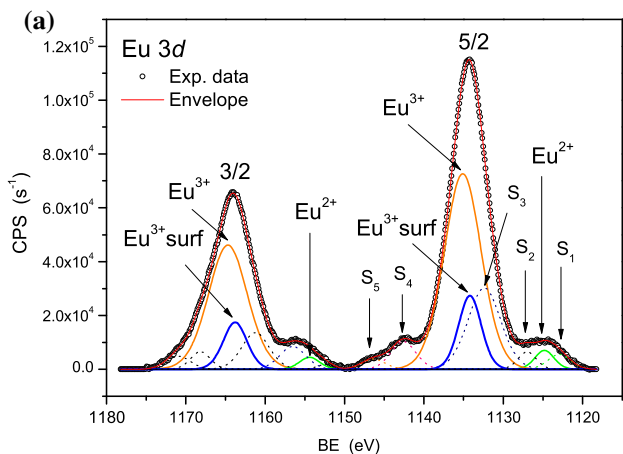
Fig. 6 The XPS spectra of **a** Eu 3d core-level doublets for the 2.5 % Eu-doped ZnO nanoparticles sample, together with the corresponding deconvolutions and fitted curves; S1 and S2 are Eu^{3+} shakedown final states features, while S3 Eu^{2+} shakeup satellite. S4 and S5 shakeup satellites may be attributed to a multiplet configuration, and a satellite feature produced by the valence band rearrangement, respectively.

b Zn 2p core-level doublets together with the corresponding deconvolutions and fitted curves for 2.5 % Eu-doped ZnO nanoparticles sample. Surface states are seen at low intensity peaks at lower BE. The inset shows the relative O 1s intensity evolution as a function of the etching time

in Fig. 6a. It is known that the rare earths elements have a complex structure of the XPS spectra containing, besides the main peaks, shakeup and shakedown like features, strongly depending on their oxidation state and neighboring elements. In our case, a detailed discussion should be done for Eu^{3+}, as well as Eu^{2+} ionic states both having its own satellite structure. The occurrence of Eu$_2$O$_3$ is clearly indicated in Fig. 6a by the two intense peaks centered at 1135.1 and 1164.7 eV for the (5/2) and (3/2) spin–orbit components, respectively. As expected, a shakedown feature is observed in the 3d doublet XPS spectra of Eu^{3+} [48–50] at around 1124 eV. It is composed of two peaks, S1 and S2 resulting from the final screening observed in our case at 1122.95 and 1127.0 eV, respectively [48]. At higher binding energies, two satellite features, S4 and S5 are observed, as well. The low intensity S4 peak at 1142.2 eV corresponds to one of the multiplet structure for the 3$d^9$4f^6 configuration [51], while S5 has rather a shakeup feature produced by the valence band rearrangement due to a sudden formation of a photohole.

Unfortunately, since the Eu^{2+} 3d core-level main peak binding energy is situated in the same energy region as the S1 and S2 shakedown final states of the Eu^{3+} 3d core-level features, it is often mistaken. Nevertheless, the overall signal can be deconvoluted considering that the Eu^{2+} 3d main peaks (both 3$d_{5/2}$ and 3$d_{3/2}$ states) are always accompanied by a satellite in the higher binding energy region separated by ∼7–8 eV. The occurrence of this double-peak structure for the divalent Eu into the ZnO host lattice is due to the large stabilization energy according to Hund rule specific for the 4f states associated to the exchange interaction between 3d and 4f unpaired electrons

in the final state [52, 53]. Thus, the Eu^{2+} main peaks were found at 1124.81 (5/2) and 1154.41 (3/2) eV, while the associated high-energy satellites are at 1132.4 and 1161.23 eV for 3$d_{5/2}$ and 3$d_{3/2}$ states, respectively.

In Fig. 6b, the XPS spectrum of the Zn 2p core-level corresponding to 2.5 mol% Eu is shown together with its deconvolution. The main peaks are positioned at 1121.9 and 1044.96 eV for 2$p_{3/2}$ and 2$p_{1/2}$ core-levels lines, respectively. At lower binding energies, less intense Zn 2p surface states peaks are observed at 1019.0 and 1041.44 eV. Two satellite shakeup features can be seen at higher binding energies.

The oxygen content of the samples does not show any significant modification as a result of the Ar ions sputtering. For instance, the inset of Fig. 6b shows the evolution of the total O 1s core-level line intensity relative to the intensity after 5 min sputtering, as a function of the etching time for the 2.5 % Eu-doped ZnO sample. We choose as reference the line intensity after the first 5 min Ar ions sputtering to avoid the effects of surface oxygen contamination. Thus, no artificial reduction of ZnO was evidenced as a result of accelerating Ar ions at 1 kV.

For quantitative determination, the integral intensities of Eu 3d and Zn 2p core—level lines were calibrated by using the corresponding real sensitivity, transmission, and electronic mean free path factors (data base of *CASA* software). All the values of the binding energies are generally subjected to ±0.3 eV variations as a result of C 1s positioning errors.

Being a composite material, for the quantitative analysis of samples containing ZnO:Eu, Eu$_2$O$_3$, and residual carbon, the escape depth corrections (attenuation lengths) are also

necessary. The weight and molar concentrations were calculated by dividing the normalized integral intensities of Eu^{3+} $3d_{5/2}$ and Zn $2p_{3/2}$ to C 1s lines by the corresponding escape depths according to Ref. [54] by using the general formula given by Cumpson and Seah [55].This formula accounts for the mean molar mass, the mean electronic number, the density, and the kinetic energy corresponding for each of the analyzed peak positions. The calculated values of the escape depth corrections were 0.46, and 0.60–0.62 for Eu_2O_3 and ZnO, respectively. The small variations of escape depth for ZnO:Eu are due to the different doping level of the samples. For the C 1s line, the escape depth was obtained 2.2 nm. The composition of ZnO:Eu samples is given in Table 1.

The XPS depth profile of Eu^{2+} and Eu^{3+} content, as resulted from the calibrated integral intensities dependences on the cumulative etching time, is presented in Fig. 7a for the 2.5 mol% Eu sample. One can observe that the Eu^{2+} ions concentration in the ZnO nanoparticles decreases in depth. It is an indication that the doping process of the ZnO nanoparticles is diffusion driven. It begins at the surface and is less efficient with respect to the inner part of the nanocrystals. The non-diffused europium excess undergoes further oxidation resulting in the formation of Eu_2O_3 nanocrystals. We have to mention that the correlation between the sputtering time and the etching process rate is possible when the sample is conductive. The effectiveness of this process is measured through monitoring the ground discharge current. In our case, with almost insulating samples, the discharge current to the ground does not reflect the rate at which the etching is produced. This is because the sample behaves like a capacitor, thus the etching rate which is accompanied by positive charge accumulation, and the ground discharging current operate with large time constant differences.

The efficiency of the doping process may be seen in Fig. 7b where the ratio between the XPS calibrated integral line intensity $I(Eu^{2+})$, associated to the ZnO doping level, and the total europium content as calculated for each sample, $I_{total} = I(Eu^{2+}) + I(Eu^{3+})$, is presented as a function of the initial europium concentration. By

increasing the initial europium concentration, the relative amount of divalent Eu substituting the ZnO matrix significantly decreases, indicating the preferential formation of the Eu_2O_3 phase. On the other hand, the absolute doping level of Eu^{2+} into ZnO can be evaluated by representing the $I(Eu^{2+})/[I(Eu^{2+}) + I(Zn_{total})]$ ratio dependence on the theoretical Eu concentration. Up to 0.5 mol% theoretical Eu concentration, the resulted Eu^{2+} doping level is almost constant, but at higher theoretical Eu concentration it increases.

Photoluminescence spectroscopy

Besides the structural and morphological consideration, the luminescent properties of the ZnO:Eu samples should be assessed in terms of emission intensity and characteristic peaks, which relate to the degree of incorporation into the lattice and the valence state of the Eu ions, respectively. In divalent, trivalent, or even with both valence states, the europium ions exhibit luminescence when present in different oxide matrices leading to simultaneous $4f \rightarrow 5d$ broad emission band and/or 4f–4f characteristic line emission [56]. The room temperature luminescence spectra for the undoped and Eu-doped ZnO nanoparticles at an excitation wavelength of 360 nm are shown in Fig. 8.

The PL spectra of all samples present a near-band edge UV band centered at 395–397 nm, attributed to the free exciton recombination. According to the literature data, the blue emission bands at 435, 454, and 469 nm for the ZnO spectrum originates from extended interstitial zinc (Zn_i), located slightly below the simple interstitial zinc state, to the valence band (VB), possible to be formed during the annealing process, resulting in a defect localization coupled with a disordered lattice [57–60]. Also, the blue emission bands at 483 and 494 nm are attributed to the intrinsic defects, such as oxygen and zinc interstitials [58]. The origin of the well-known green emission of ZnO nanoparticles around 560 nm was intensively studied and it strongly depends on the surface morphology and the grain structure [61, 62]. Ye et al. [63] related that this band originates from the radiative recombination of the V_O^x (electron from the conduction band is trapped by V_O^+ forming an instable V_O^x center) with the hole from the VB. When V_O^{++} (formed when V_O^+ traps a hole from the grain surface) are the dominant native defects, they trap a photoexcited electron from the CB and yield photons with an energy value around 2.2 eV (560 nm). The luminescent properties are influenced by the addition of the europium ions into the ZnO matrix. The observed visible emission bands are different, meaning that both the specific emission attributed to the $4f^7–4f^65d^1$ for Eu^{2+} and $^5D_0 \rightarrow {}^7F_2$ for Eu^{3+} transitions and the emission induced by the existence

Table 1 The calculated values for the composition of the ZnO:Eu samples

Nominal Eu^{3+} (mol%)	Eu^{2+} (mol%)	Composition					
		ZnO:Eu		Eu_2O_3		Residual C	
		mol%	wt%	mol%	wt%	mol%	wt%
0.1	0.097	98.27	99.36	0.10	0.41	1.60	0.22
0.5	0.100	97.26	98.67	0.25	0.99	2.40	0.33
1	0.204	98.69	97.58	0.67	2.35	0.64	0.08
2.5	0.279	95.06	86.54	4.42	13.40	0.50	0.05
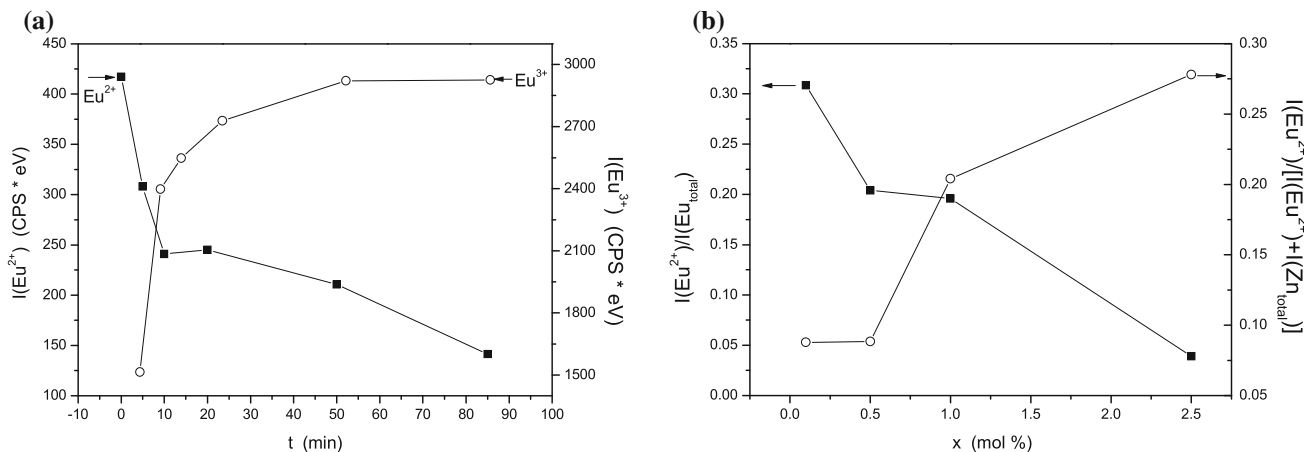
Fig. 7 **a** The XPS depth profile of Eu^{2+} and Eu^{3+} contents for 2.5 mol% Eu analyzed by using Ar ions etching and **b** Eu^{2+} content versus Eu_{total} content as function of Eu concentration and $Eu^{2+}/(Eu^{2+} + Zn_{total})$ as function of Eu concentration
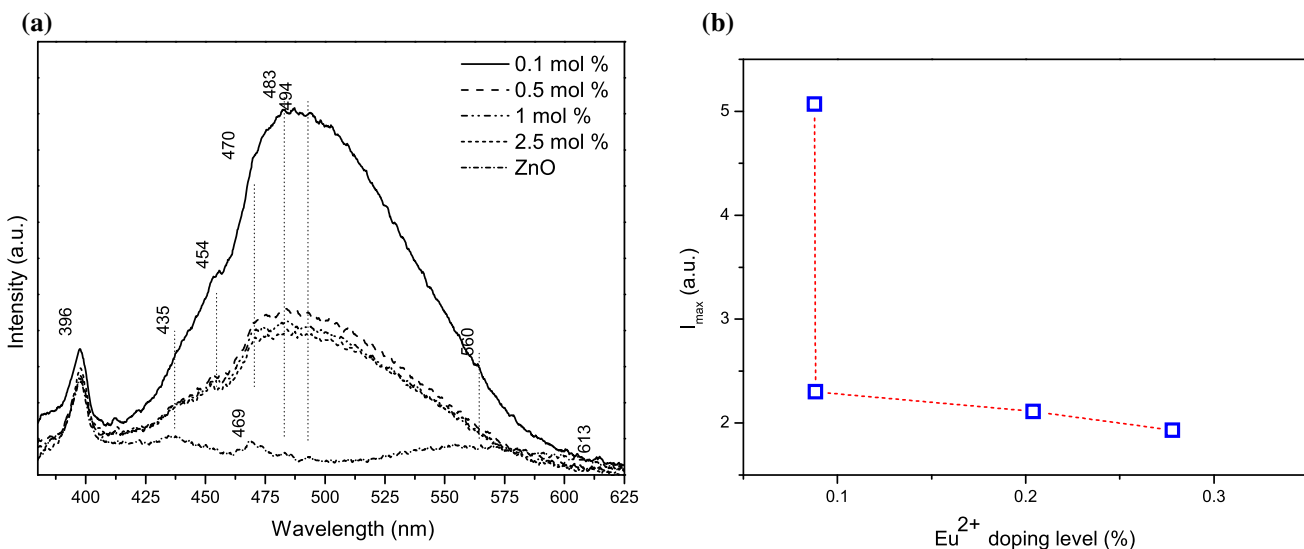
Fig. 8 PL spectra of ZnO and Eu-doped ZnO nanoparticles ($\lambda_{exc.} = 360$ nm)

of multiple defects in the ZnO nanoparticles are present. One can observe that the PL spectra of Eu-doped ZnO samples present similarities, but the intensities of the main emission bands decrease with the increase of europium concentration from 0.1 to 2.5 mol%.

The peak intensities centered at 435, 454, 470, 483, and 494 nm were strongly influenced by the presence of europium ion. The most intense emission was registered for the 0.1 mol% europium sample. The increase of Eu concentration in the ZnO samples is accompanied by the decrease of the emission. Also, it is well known that the $4f^7$–$4f^65d^1$ transition of Eu^{2+} presents a broad emission centered at 530 nm. The asymmetric allure for all the ZnO:Eu spectra can be explained by the presence of this latter Eu^{2+} emission band [11, 64–66]. The low red PL

emission peak at 613 nm observed in ZnO:Eu samples is associated to the $^5D_0 \rightarrow {}^7F_2$ transition of the Eu^{3+} ions. This low intensity emission is due to the fact that most of the energy of the 360 nm excitation photons, being transferred to higher excited electronic states, is lost through ZnO defects by radiative recombinations [50].

The decrease of the PL intensity may be understood in terms of two processes: (i) quenching of the PL due to the Eu_2O_3 formation and (ii) "quenching" produced by increasing the Eu^{2+} doping concentration of ZnO known as concentration quenching [63]. In Fig. 8b, it is represented the maximum of PL intensity (483 nm) as a function of the Eu^{2+} doping level from Table 1. It can be noticed that, although samples with nominal 0.1 and 0.5 % have the same Eu^{2+} concentration, their PL response differs

significantly. The difference between samples is given by the increased quantity of Eu_2O_3 secondary phase formation in the sample with 0.5 mol% Eu nominal concentration with respect to 0.1 mol% Eu sample. Thus, the first quenching process may be attributed to the Eu_2O_3 crystallite formation on the surface of ZnO. Here the Eu^{3+} ions act as non-radiative decay centers. The linear reduction of the PL response for samples with larger doping levels may be further seen as due to already mentioned concentration quenching. In the same time, the decrease of ZnO crystallite size with the increase of Eu nominal concentration was already mentioned. This process is accompanied by an increase of the ZnO surface defects. It is already known that these defects act as radiative decay centers, thus reducing the quenching effect due to Eu_2O_3 formation, explaining the slower decrease of PL dependence in the 0.1–0.3 mol% Eu domain.

Conclusions

Eu-doped ZnO nanoparticles have been synthesized by a wet chemical synthesis route using the SimAdd technique. The full understanding of decomposition mechanism of the as-obtained oxalate precipitate was achieved based on the thermal analysis correlated with the evolved gas analysis and FTIR spectroscopy. The XRD studies reveal the formation of a hexagonal wurtzite-type structure. The presence of Eu_2O_3 cubic structure can be observed up to 0.5 mol% Eu, suggesting that the solubility of the divalent or trivalent Eu into the ZnO lattice is limited. The formation of Eu_2O_3 secondary phase at higher Eu concentration is sustained by Raman spectroscopy, as well. It is worthwhile mentioning that in the wavenumber range 2000–8000 cm^{-1} only the Eu-doped ZnO nanoparticles present bands and these bands are specific to Eu_2O_3. Also, the Raman and XPS investigations suggest that at smaller europium concentration, 0.1 mol%, a part of the Eu^{3+} ions are reduced to Eu^{2+} and incorporated into the ZnO lattice. According to the Raman spectra, the divalent component of europium is expected, and corresponds to the europium ions that substitute the Zn^{2+} ions into the ZnO host lattice. On the other side, the presence of Eu^{3+} ions may be either due to the interstitial incorporation of Eu ions into the ZnO matrix, or to the formation of Eu_2O_3 as a secondary phase. The TEM investigations of the Eu-doped ZnO samples illustrate the presence of aggregates with different shapes and dimensions formed by agglomerated spherical and polyhedral nanoparticles with sizes ranging from 20 to 120 nm. The PL measurements sustain the presence of both divalent and trivalent europium ions into the ZnO host lattice and, at the same time, an increase of its defects density induced by the dopant presence. In summary,

following this wet chemical synthesis route, the partial reduction of the $Eu^{3+} \rightarrow Eu^{2+}$ ions was evidenced by complementary XRD, Raman, XPS, and PL investigation methods. The possibility to tune the luminescence emission of the Eu-doped zinc oxide by controlling the Eu^{2+}/Eu^{3+} ratio was pointed out by this study. Supplementary experiments have already been developed in order to increase the Eu^{2+} concentration by the thermal treatment of zinc oxalate-type precursor under reducing atmosphere. In this context, the possibility to synthesize phosphors with targeted luminescence emission can be achieved.

References

1. Bagnall DM, Chen YF, Zhu Z, Yao T, Koyama S, Shen M, Goto T (1997) Optically pumped lasing of ZnO at room temperature. Appl Phys Lett 70:2230–2232
2. Jiao SJ, Zhang ZZ, Lu YM, Shen DZ, Yao B, Zhang JY, Li BH, Zhao DX, Fan XW, Tang ZK (2006) ZnO p - n junction light-emitting diodes fabricated on sapphire substrates. Appl Phys Lett 88:031911. doi:10.1063/1.2166686
3. Xiong G, Pal U, Serrano JG (2007) Correlations among size, defects, and photoluminescence in ZnO nanoparticles. J Appl Phys 101:024317–1–024317–6. doi:10.1063/1.2424538
4. Vaja F, Comanescu C, Oprea O, Ficai D, Guran C (2012) Effects of ZnO nanoparticles on the wet scrub resistance and photocatalytic properties of acrylic coatings. Rev Chim 63(7):722–726
5. Behnajady MA, Modirshahla N, Ghazalian E (2011) Synthesis of ZnO nanoparticles at different conditions: a comparison of photocatalytic activity. Dig J Nanomater Biostruct 6:467–474
6. Kakiuchi K, Hosono E, Fujihara S (2006) Enhanced photoelectrochemical performance of ZnO electrodes sensitized with N-719. J Photochem Photobiol, A 179:81–86
7. Djerdj I, Garnweitner G, Arčon D, Pregelj M, Jagličić Z, Niederberger M (2008) Diluted magnetic semiconductors: Mn/Co-doped ZnO nanorods as case study. J Mater Chem 18:5208–5217
8. Hays J, Reddy KM, Graces Ny, Engelhard Mh, Shuttanandan V, Luo M, Xu C, Giles NC, Wang C, Thevuthasan S, Punnoose A (2007) Effect of Co doping on the structural, optical and magnetic properties of ZnO nanoparticles. J Phys: Condens. Matter 19:266203
9. Litton CW, Reynolds DC, Collins TC (2011) Zinc oxide materials for electronic and optoelectronic device applications. Wiley, New York. ISBN 978-0-470-51971-4
10. Ischenko V, Polarz S, Grote D, Stavarache V, Fink K, Driess M (2005) Zinc oxide nanoparticles with defects. Adv Funct Mater 15:1945–1954
11. Petersen J, Brimont C, Gallart M, Schmerber G, Gilliot P, Ulhaq-Bouillet C, Rehspringer JL, Colis S, Becker C, Slaoui A, Dinia A (2010) Correlation of structural properties with energy transfer of Eu-doped ZnO thin films prepared by sol-gel process and magnetron reactive sputtering. J Appl Phys 107:123522-1–123522-6
12. Yanmin Q, Xinbo Z, Xiao Y, Yan C, Hai G (2009) Photoluminescent properties of $Sr_2SiO_4:Eu^{3+}$ and $Sr_2SiO_4:Eu^{2+}$ phosphors

prepared by solid-state reaction method. J Rare Earths 27:323–326

13. Kumar V, Kumar V, Som S, Duvenhage MM, Ntwaeaborwa OM, Swart HC (2014) Effect of Eu doping on the photoluminescence properties of ZnO nanophosphors for red emission applications. Appl Surf Sci 308:419–430

14. Yang L, Jiang Z, Dong J, Pan A, Zhuang X (2014) The study on crystal defects-involved energy transfer process of Eu^{3+} doped ZnO lattice. Mater Lett 129:65–67

15. Yadav RS, Pandey AC, Sanjay SS (2009) Optical properties of europium doped bunches of ZnO nanowires synthesized by co-precipitation method. Chalcogenide Lett 6:233–239

16. Chowdhury PS, Saha S, Patra A (2004) Influence of nanoenvironment on luminescence of Eu^{3+} activated SnO_2 nanocrystals. Solid State Commun 131:785–788

17. Ebisawa K, Okuno T, Abe K (2008) Photoluminescence properties of Eu3+-doped ZnO nanoneedles. Jpn Appl Phys 47:7236–7238

18. Fang TH, Chang YS, Ji LW, Prior SD, Eater W, Chen KJ, Fang CF, Fang CN, Shen ST (2009) Photoluminescence characteristics of ZnO doped with Eu3+ powders. J Phys Chem Solids 70:1015–1018

19. Li M, Xu J, Chem X, Zhang X, Wu Y, Li P, Niu X, Luo C, Li L (2012) Structural and optical properties of cobalt doped ZnO nanocrystals. Superlattices Microstruct 52:824–833

20. Hammad TM, Salem JK, Harrison R (2010) The influence of annealing temperature on the structure, morphologies and optical properties of ZnO nanoparticles. Superlattices Microstruct 47:335–340

21. Raj CJ, Joshi RK, Varma BR (2011) Synthesis from zinc oxalate, growth mechanism and optical properties of ZnO nano/micro structures. Cryst Res Technol 46:1181–1188

22. Bohle DS, Spina CJ (2010) Controlled Co(II) doping of zinc oxide nanocrystals. J Phys Chem C 114(42):18139–18145

23. Gaudon M, Toulemonde O, Demourgues A (2007) Green coloration of Co-doped ZnO explained from structural refinement and bond considerations. Inorg Chem 46:10996–11002

24. Liu Y, Luo W, Li R, Liu G, Antonio MR, Chen X (2008) Optical spectroscopy of Eu^{3+} doped ZnO nanocrystals. J Phys Chem C 112:686–694

25. Ambrožič G, Škapin SD, Žigon M, Orel ZC (2010) The synthesis of zinc oxide nanoparticles from zinc acetylacetonate hydrate and 1-butanol or isobutanol. J Coll Interface Sci 346:317–323

26. Kiomarsipour N, Razavi RS (2013) Hydrothermal synthesis and optical property of scale- and spindle-like ZnO. Ceramics Int 39:813–818

27. Hang TT, Anh TX, Huy PT (2009) Controlled synthesis and luminescence of Eu doped ZnO nanowires and nanorods via hydrothermal method. J Phys: Conf Ser 187:012022. doi:10.1088/1742-6596/187/1/012022

28. Vasile OR, Andronescu E, Ghitulica C, Vasile BS, Oprea O, Vasile E, Trusca R (2012) Synthesis and characterization of nanostructured zinc oxide particles synthesized by pyrosol method. J Nanopart Res 14:1269. doi:10.1007/s11051-012-1269-7

29. Dinu E, Siebert E, Andronescu E, Djurado E, Dessemond L, Ghitulica C (2008) Nanocrystallites obtained through the pyrosol method. Phys Status Solidi A 205:1488–1493

30. Lin JC, Lee C, Ho KC (2012) Zinc oxide synthesis via a microemulsion technique: morphology control with application to dye-sensitized solar cells. J Mater Chem 22:1270–1273

31. Dolcet P, Casarin M, Maccato C, Bovo L, Ischia G, Gialanella S, Mancin F, Tondello E, Gross S (2012) Miniemulsions as chemical nanoreactors for the room temperature synthesis of inorganic crystalline nanostructures: ZnO colloids. J Mater Chem 22:1620–1626

32. Bhargava RN, Chhabra V, Som T, Ekimov A, Taskar N (2002) Quantum Confined Atoms of Doped ZnO Nanocrystals. Phys Status Solidi 229:897–901

33. He S, Zheng M, Yao L, Yuan X, Li M, Ma L, Shen W (2010) Preparation and properties of ZnO nanostructures by electrochemical anodization method. Appl Surf Sci 256:2557–2562

34. Ding L, Zhang L, Fan L (2013) Electrochemical route to the synthesis of ZnO microstructures: its nestlike structure and holding of Ag particles. Nano Res Lett 8:78. doi:10.1186/1556-276X-8-78

35. Yukas B, Yang P (2009) Nanowire-based all-oxide solar cells. J Am Chem Soc 131:3756–3761

36. Toloman D, Mesaros A, Popa A, Raita O, Silipa TD, Vasile BS, Pana O, Giurgiu LM (2013) Evidence by EPR of ferromagnetic phase in Mn-doped ZnO nanoparticles annealed at different temperatures. J Alloys Compd 551:502–507

37. Suwanboon S, Amornpitoksuk P, Sukolrat A (2011) Dependence of optical properties on doping metal, crystallite size and defect concentration of M-doped ZnO nanopowders (M = Al, Mg, Ti. Ceram Int 37:1359–1365

38. Choudhury T, Saied SO, Sullivan JL, Abbot AM (1989) Reduction of oxides of iron, cobalt, titanium and niobium by low-energy ion bombardment. J Phys D Appl Phys 22:1185–1195

39. Muresan L, Popovici EJ, Bica E, Cadis AI, Perhaita I, Tudoran LB (2012) Investigation of thermal decomposition of yttrium-aluminium-based precursors for YAG phosphors. J Therm Anal Calorim 110:341–348

40. Saponar A, Popovici EJ, Perhaita I, Nemes G, Cadis AI (2012) Thermal behaviour of some ester derivates of p-tert-butyl calyx[n]arene. Therm Anal Calorim 110:349–356

41. Shannon RD (1976) Revized effective ionic radii and systematic studies of interatomic distances in halides and chalcogenides. Acta Cryst A32:751–767

42. Husain S, Alkhtaby LA, Giorgetti E, Zoppi A, Miranda MM (2014) Effect of Mn doping on structural and optical properties of sol gel derived ZnO nanoparticles. J Lumin 145:132–137

43. Kumar PS, Paik P, Raj AD et al (2012) Biodegradability study and pH influence on growth and orientation of ZnO nanorods via aqueous solution process. Appl Surf Sci 258:6765–6771

44. Hassan NK, Hashim MR (2013) Flake-like ZnO nanostructures density for improved absorption using electrochemical deposition in UV detection. J Alloys Compd 577:491–497

45. Wang JB, Huang GJ, Zhong XL, Sun LZ, Zhou YC (2006) Raman scattering and high temperature ferromagnetism of Mn-doped ZnO nanoparticles. Appl Phys Lett 88:252502. doi:10.1063/1.2208564

46. Avram D, Rotaru C, Cojocaru B, Sanchez-Dominiquez M, Florea M, Tiseanu C (2014) Heavily impregnated ceria nanoparticles with europium oxide: spectroscopic evidences for homogenous solid solutions and intrinsic structure of Eu3+-oxygen environments. J Mater Sci 49:2117–2126

47. Elen K, Kelchtermans A, Van den Rul H, Peeters R, Mullens J, Hardy A, Van Bael MK (2011) Comparison of two novel solution-based routes for the synthesis of equiaxed ZnO nanoparticles. J Nanomater, ID:390621(pp 6)

48. Schneider WD, Laubschat C, Nowik I, Kaindl G (1981) Shake-up excitations and core-hole screening in Eu systems. Phys Rev B 24:5422–5425

49. Mercier F, Alliot C, Bion L, Thromat N, Toulhoat P (2006) XPS study of Eu(III) coordination compounds: core levels binding energies in solid mixed-oxo-compounds $Eu_mX_xO_y$. J Electron Spectrosc Relat Phenom 150:21–26

50. Leostean C, Stefan M, Pana O, Cadis AI, Suciu RC, Silipas TD, Gautron E (2013) Properties of Eu doped TiO2 nanoparticles prepared by using organic additives. J Alloys Compd 575:29–39

51. Cho EJ, Oh SJ (1999) Surface valence transition in trivalent Eu insulating compounds observed by photoelectron spectroscopy. Phys Rev B 59:R15613–R15616

52. Cho EJ, Oh SJ, Imada S, Suga S, Suzuki T, Kasuya T (1995) Origin of the high-binding-energy structure in the 3d core-level spectra of divalent Eu compounds. Phys Rev B 51:10146–10149

53. Laubschat C, Perscheid B, Schneider WD (1983) Final-state effects and surface valence in Eu—transition-metal compounds. Phys Rev B 28:4342–4348

54. Pana O, Soran ML, Leostean C, Macavei S, Gautron E, Teodorescu CM, Gheorghe N, Chauvet O (2012) Interface charge transfer in polypyrrole coated perovskite manganite magnetic nanoparticles. J Appl Phys 111:044309. doi:10.1063/1.3686662

55. Cumpson PJ, Seah MP (1997) Elastic scattering corrections in AES and XPS. II. estimating attenuation lengths and conditions required for their valid use in overlayer/substrate experiments. Surf Interface Anal 25:430–446

56. Avci N, Korthout K, Newton M, Smet P, Poelman D (2012) Valence states of europium in CaAl2O4: Eu phosphors. Opt Mater Express 2:321–330

57. Liu DH, Liao L, Li JC, Guo HX, Fu Q (2005) Preparation and photoluminescence of ZnO nanostructures by thermal evaporation growth without catalysts. Mater Sci Eng B 121:77–80

58. Ghosh A, Deshpande NG, Gudage YG, Joshi RA, Sagade AA, Phase DM, Sharma R (2009) Effect of annealing on structural and optical properties of zinc oxide thin film deposited by successive ionic layer adsorption and reaction technique. J Alloys Compd 469:56–60

59. van Dijken A, Meulenkamp EA, Vanmaekelbergh D, Meijerink A (2000) The kinetics of the radiative and nonradiative processes in nanocrystalline ZnO particles upon photoexcitation. J Phys Chem B 104:1715–1723

60. Zeng H, Duan G, Li Y, Yang S, Xu X, Cai W (2010) Blue luminescence of ZnO nanoparticles based on non-equilibrium processes: defect origins and emission controls. Adv Funct Mater 20:561–572

61. Popa M, Mesaros A, Mereu RA, Suciu R, Vasile BS, Gabor MS, Ciontea L, Petrisor T (2013) Optical properties correlated with morphology and structure of TEAH modified ZnO nanoparticles via precipitation method. J Alloys Compd 574:255–259

62. Sharma PK, Pandey AC, Zolnierkiewicz G, Gustos N, Rudowicz C (2009) Relationship between oxygen defects and the photoluminescence property of ZnO nanoparticles: a spectroscopic view. J Appl Phys 106:094314. doi:10.1063/1.3256000

63. Ye JD, Gu SL, Qin F, Zhu SM, Liu SM, Zhou X, Liu W, Hu LQ, Zhang R, Shi Y, Zheng YD (2005) Correlation between green luminescence and morphology evolution of ZnO films. Appl Phys A 81:759–762

64. Luo M, Cheng K, Weng W, Song C, Du P, Shen G, Xu G, Han G (2009) Enhanced luminescence of Eu-doped TiO2 nanodots. Nanoscale Res Lett 4:809–813

65. Chen W, Malm JO, Zwiller V, Huang Y, Liu S, Wallenberg R, Bovin JO, Samuelson L (2010) Energy structure and fluorescence of Eu 2^+ in ZnS: Eu nanoparticles. Phys Rev B 61:11021–11024

66. Lupan O, Pauporte T, Viana B, Ascheoug P, Ahmadi M, Cueya BR, Rudzevich Y, Lin Y, Chow L (2013) Eu-doped ZnO nanowire arrays grown by electrodeposition. Appl Surf Sci 282:782–788